Available online at www.sciencedirect.com

ScienceDirect

Proceedings of the Combustion Institute 36 (2017) 1637–1644

Proceedings of the Combustion Institute

www.elsevier.com/locate/proci

A criterion to distinguish autoignition and propagation applied to a lifted methane–air jet flame

O. Schulz [a,*], T. Jaravel [b], T. Poinsot [b], B. Cuenot [b], N. Noiray [a]

[a] *CAPS Laboratory, Department of Mechanical and Process Engineering, ETH Zurich, Zurich 8092, Switzerland*
[b] *CERFACS, 42 Avenue G. Coriolis, Toulouse Cedex 01 31057, France*

Received 3 December 2015; accepted 7 August 2016
Available online 10 October 2016

Abstract

This numerical study deals with the distinction between autoignition and propagation driven reaction zones using an autoignition index (*AI*). It allows a clear identification of the two burning regimes based on the relative contribution of two reactions for hydroperoxyl (HO_2) chemistry. *AI* was applied to a lifted methane–air jet in a hot (1350 K) vitiated coflow, namely the Cabra flame configuration. Large Eddy Simulation (LES) were performed using the Dynamic Thickened Flame model (DTF) with an Analytically Reduced Chemistry (ARC) mechanism with 22 transported species, as well as 18 species in Quasi-Steady State (QSS) approximation. A detailed validation of the numerical methods is presented. Comparisons with experimental data are in good agreement for mixture fraction, temperature and species mass fractions for both a fine and a coarse mesh. In a detailed analysis of the flame structure, *AI* identifies autoignition as dominant over propagation at the flame base. Autoignition pockets are close to the lean most reactive mixture fraction. Lean and rich propagation is recognized to dominate in regions located at higher mixture fractions closer to the centerline with significantly higher heat release rates compared to autoignition.

Keywords: Autoignition; LES; Lifted flame; Thickened flame model; Reduced chemistry

1. Introduction

The design complexity of modern combustors is constantly increasing – for example in land-based gas turbine applications, sequential combustion or axial staging concepts [1–3] involving Moderate or Intense Low-oxygen Dilution (MILD) [4], or Exhaust Gas Recirculation (EGR) architectures [5]. These technology step-changes are driven by the demand for lower pollutant emissions, higher efficiency and higher fuel and operational flexibility. Recent progress in experimental methods and in Computational Fluid Dynamics enable more robust design and optimization of these new concepts. Still there are often situations, for instance, during prototypes testing phases, where a qualitative and quantitative understanding of the combustion process is lacking. The combustion regime in practical systems is one of these important questions, as premixed

* Corresponding author.
E-mail address: oschulz@ethz.ch (O. Schulz).

http://dx.doi.org/10.1016/j.proci.2016.08.022
1540-7489

Table 1
Numerical studies applied to the Cabra flame classified according to their combustion model (PDF – Probability Density Function, CMC – Conditional Moment Closure, TF – Thickened Flame).

		PDF	CMC	TF
Tabulated Chemistry	RANS	[15–17]	[11]	–
	LES	[12,18–20]	–	–
Full Chemistry	RANS	[22]	–	–
	LES	–	[23]	–
Reduced Chemistry	RANS	[13,24]	–	–
	LES	–	[25]	**This Work**

or partially-premixed propagation, non-premixed combustion or autoignition, have a direct impact on the performances and stability of the burner.

With the aim of distinguishing between premixed and non-premixed flames, Yamashita et al. [6] derived the flame index (*FI*). Another criterion is proposed in this paper, that allows to discriminate between propagating and auto-igniting reaction zones. It is built on the reaction rate flux analysis proposed by Yoo et al. [7], who identified the dominant role of autoignition at the flame base of a hydrogen jet flame by analyzing the chemistry of hydroperoxyl (HO_2) and hydroxyl (OH). This is particularly relevant for flames stabilized in vitiated flows encountered for instance in modern turbomachinery applications – one can refer to previous experimental work [8–10] or numerical studies [7,11,12] on that topic. The here proposed criterion was applied to the lifted methane–air jet, that has been experimentally and numerically investigated by Cabra et al. [13].

This well-documented experimental work has been used for development and validation purposes of several combustion models, summarized in Table 1. The widely used tabulated flamelet approach originally proposed by Peters [14] has been providing encouraging results for Reynolds-averaged Navier–Stokes (RANS) [15–17] and Large Eddy Simulation (LES) modeling [12,18–20]. However one drawback is the augmented complexity of the look-up table with more practical combustion applications. Cooling, dilution or fuel injection with different compositions can result in three or higher stream mixing problems, adding a number of parameters to the look-up table and therefore considerably increasing the computing time [21].

As an alternative, a 44 species detailed chemistry scheme, combined with a transported Probability Density Function (PDF) was used by Gkagkas and Lindstedt [22] in RANS simulations. Their work gives insight into the dominant reactions for the pre- and autoignition process. Martinez and Kronenburg used a detailed skeletal mechanism with 44 species [23] and reduced mechanisms [25], both in combination with a CMC approach to perform LES. Such methods still lead to important computing time to resolve the stochastic nature of the reacting turbulent flow.

In the present paper, for the first time the Thickened Flame (TF) model [26] in combination with reduced chemistry is used to simulate the Cabra flame. Objectives are to evaluate the performances of this less demanding approach in terms of computing time, and to analyze the flame structure in view of identifying the combustion regimes.

The current paper is structured as follows: In the following section, the criterion to distinguish between autoignition and propagation is presented. In the third section, the Cabra flame configuration is introduced and numerical approaches are validated against the experiment. In the last part, the autoignition index (*AI*) is applied to the Cabra flame configuration and an analysis of the flame structure and stabilization mechanism is proposed.

2. A criterion to distinguish between autoignition and propagation

A reaction rate flux analysis of HO_2 chemistry to distinguish between propagation and autoignition is presented. This analysis is based on the findings of Gkagkas and Lindstedt [22], who showed that the formation of the HO_2 radical is mainly due to (keeping the same reaction numbering as in [22]):

$$O_2 + H(+M) \Longleftrightarrow HO_2(+M) \quad \text{(R5)}$$

$$CHO + O_2 \Longleftrightarrow CO + HO_2 \quad \text{(R34)}$$

Consumption of HO_2 is through the following reactions:

$$HO_2 + H \Longleftrightarrow OH + OH \quad \text{(R6)}$$

$$HO_2 + OH \Longleftrightarrow H_2O + O_2 \quad \text{(R8)}$$

$$CH_3 + HO_2 \Longleftrightarrow CH_3O + OH \quad \text{(R74)}$$

Figure 1 shows the HO_2 reaction rates ($\dot{\omega}_{HO_2}$) profiles of the above reactions for three different 1-D simulations representing different burning regimes, namely propagation (a) and autoignition (d), as well as a transitional case between the two (c). Indeed, below a minimum equivalence ratio a freely propagating flame cannot be observed anymore and autoignition of the fresh mixture starts to dominate [12]. Note the change in spatial scale between propagation and autoignition regimes. The 1-D propagating laminar flame (a) is stabilized by imposing the velocity of the laminar flame speed $s_L = 3.2$ m/s at the inlet, whereas the position of the reaction zone of simulation (d) is determined by the inlet velocity and the autoignition time of the mixture imposed at the inlet. The inlet velocity

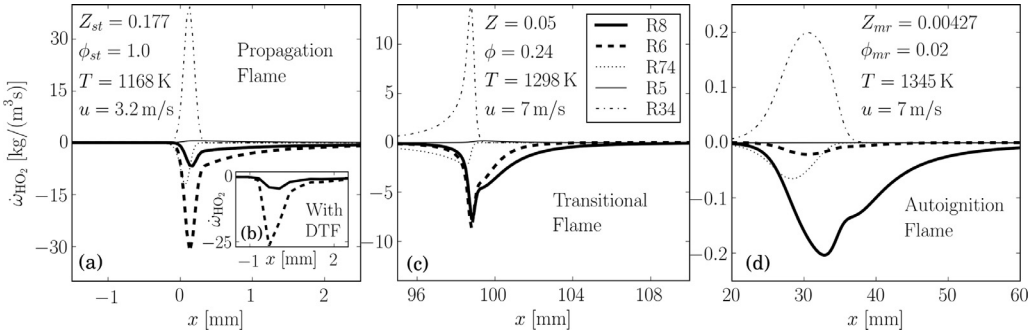

Fig. 1. (a–d) Profiles of dominant reaction rates contributing to HO_2 source term in enlargements of reaction zones. (a), (c), (d): derived on DNS mesh. (b): inset plot in (a) derived from LES with the DTF (Dynamic Thickened Flame) model. (a), (b): premixed propagation flame at stoichiometry Z_{st}. (c): transitional case between propagation and autoignition. (d): autoignition flame at most reactive mixture fraction Z_{mr}.

was set to 7 m/s, which is a characteristic value for the outer shear layer of the jet close to the reaction zone. Compositions and temperatures correspond to the mixture fractions that are reported in the Cabra flame, and are indicated in the figures, with the subscripts *st* denoting stoichiometric values (a) and *mr* the most reactive value for the considered mixture and temperature (d), defined as the mixture fraction with the smallest autoignition delay derived from Perfectly Stirred Reactor (PSR) simulations. Note that throughout the paper the mixture fraction definition formulated by Bilger et al. [27] is used. One can also see in Fig. 1b (inset in Fig. 1a) the contributions from R6 and R8 extracted from a LES case with Dynamic Thickened Flame (DTF) model and identical boundary conditions as (a).

Going from propagation at stoichiometry in Fig. 1a to very lean autoignition in Fig. 1d, the reaction rates globally decrease by approximately two orders of magnitude. More importantly, the relative contribution of R8 and R6 changes significantly: in (a), reaction R6 is the major contributor to HO_2 consumption compared to R8; when decreasing the equivalence ratio to $\phi = 0.24$ (c), reactions R8 and R6 reach a comparable level; finally in the auto-igniting case (d), the contribution of reaction R6 to $\dot{\omega}_{HO_2}$ is relatively small compared to R8. Note that R74, R5 and R34 do not significantly change in their relative contribution for the three cases.

Based on the previous observations an autoignition index (*AI*) was derived:

$$AI = \left| \frac{\dot{\omega}^{(R8)}_{HO_2}}{\dot{\omega}^{(R8)}_{HO_2} + \dot{\omega}^{(R6)}_{HO_2}} \right|. \quad (1)$$

It is considered that a region is in an autoignition regime when the HO_2 reaction rate of R8 ($\dot{\omega}^{(R8)}_{HO_2}$) is locally dominating over the one of R6 ($\dot{\omega}^{(R6)}_{HO_2}$). Thus the criterion $AI > 0.5$ is used to identify autoignition regions in the following.

Note that in the present work AI is validated for the Cabra flame conditions. As shown for example in [28] dominant reactions can change at higher pressure and varying temperatures. Therefore one should examine the validity of AI with changing conditions and if necessary redefine the index using different reaction rates.

3. The Cabra flame configuration and numerical methods validations

3.1. Experimental setup

The Cabra flame configuration [13] consists of a cold central fuel jet with a diameter of $d = 4.57$ mm into a vitiated hot coflow ($D_{co} = 210$ mm) operated at atmospheric conditions. For the baseline case the CH_4/air mixture is injected at $T_{jet} = 320$ K with a bulk velocity of $u_{jet} = 100$ m/s ($Re = 28,000$) and the following composition in mole fractions: $X_{jet,CH_4} = 0.33$, $X_{jet,O_2} = 0.15$, $X_{jet,N_2} = 0.52$, corresponding to an equivalence ratio ϕ of 4.

The hot coflow is generated by 2200 small lean premixed H_2/air flames 70 mm upstream of the fuel jet injector. For the baseline case the coflow boundary conditions measured at one jet diameter downstream of the jet nozzle are the following: $T_{co} = 1350$ K, $u_{co} = 5.4$ m/s ($Re = 23,300$), $X_{co,O_2} = 0.12$, $X_{co,N_2} = 0.73$, $X_{co,H_2O} = 0.15$.

Single point measurements of temperature and major species concentrations were performed using the Raman–Rayleigh scattering technique.

3.2. Numerical setup and validations

The 3-D computational domain extends from the jet nozzle tip to 90 *d* in axial and to 28 *d* in radial direction. The flow-through time is estimated as 90 d/u_{jet}. Two different unstructured meshes were used, a fine mesh with 10.6 million nodes and a

characteristic cell size of 0.3 mm inside the flame front, and a coarser mesh with 2.7 million nodes and a characteristic cell size of 0.7 mm. LES were performed using AVBP, an explicit cell-vertex parallel code solving compressible reacting flows [29]. The accuracy in space and time is of third order using the numerical scheme TTGC [30]. For subgrid Reynolds stress modeling the WALE approach [31] was used. At the inlet, a fully developed turbulent pipe flow mean profile was imposed along with turbulent velocity fluctuations of intensity $u'/u_{jet} = 5 \times 10^{-4}$. The outer walls were considered as adiabatic with slip condition and the nozzle tip was treated as an adiabatic non-slipping wall. The Navier–Stokes Characteristic Boundary Conditions formulation [32] was used at the inlet and outlet.

The CPU cost for one flow-through time is about 46,000 CPU hours for the fine mesh and 9000 CPU hours for the coarse mesh.

3.2.1. Chemistry description

The chemistry is described by a reduced mechanism [33] derived from the GRI211 mechanism [34]. Compared to the original detailed mechanism, 9 species, namely HCCOH, C_2H, CH_2CO, CH_2OH, CN, NH_3, H_2CN, HCNN and Ar were removed. In addition the Quasi-Steady State approximation was applied to 18 species, leading to an analytical expression of their concentration without solving their transport equation. In the resulting Analytically Reduced Chemistry (ARC), named ARC_22_GRI211 mechanism, 22 transported species remain, namely: N_2, H, H_2, O, O_2, OH, H_2O, H_2O_2, HO_2, CO, CH_2O, CH_3, CH_3OH, C_2H_2, CH_4, C_2H_6, C_2H_4, CO_2, NO, HCN, NO_2 and N_2O.

The ARC_22_GRI211 scheme was validated on two test cases: (i) a stabilized propagating laminar premixed flame at stoichiometry (same case as in Fig. 1a) and (ii) a Perfectly Stirred Reactor (PSR), representative of the autoignition case with the same conditions as in Fig. 1d. Detailed chemistry simulations were conducted with CANTERA [36], whereas reduced chemistry results were obtained with AVBP on a 1-D, fully resolved mesh.

Figure 2 compares axial profiles of major (CH_4, O_2, CO_2, CO) and minor (OH, HO_2) species mass fractions together with temperature for the stoichiometric propagating premixed flame obtained with the detailed and reduced mechanisms. Excellent agreement is obtained for all species and temperature, leading to a first validation of the reduced scheme.

The temperature and species mass fractions evolution over time are presented in Fig. 3 for the PSR autoignition case. Again species and temperature profiles are well captured by the reduced scheme, with however some over-estimation of the autoignition delay by around 10% with the reduced scheme. This corresponds to an initial temperature difference of 9 K and was considered acceptable for the purpose of this study.

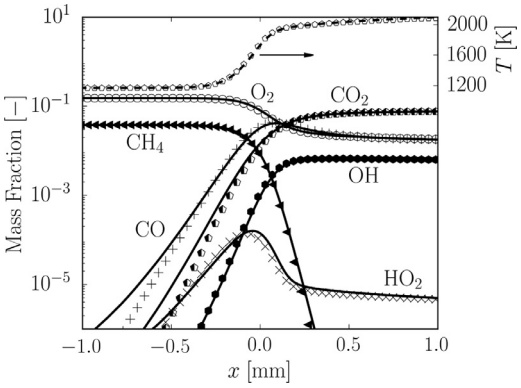

Fig. 2. Profiles of mass fractions and temperature of a stoichiometric 1-D propagating premixed flame (same case as in Fig. 1a) calculated with detailed (lines, CANTERA) and reduced chemistry (symbols, AVBP).

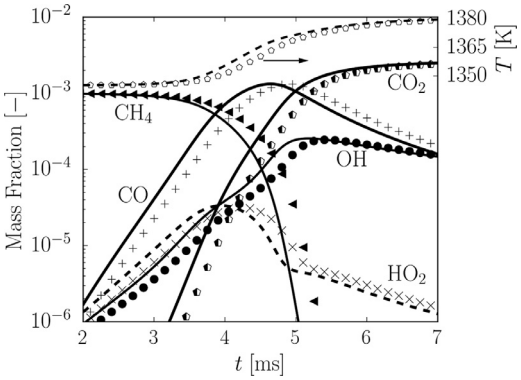

Fig. 3. Temporal evolution of mass fractions and temperature in a Perfectly Stirred Reactor (PSR) (same conditions as in Fig. 1d) calculated with detailed (lines, CANTERA) and reduced chemistry (symbols, AVBP).

3.2.2. Turbulent combustion modeling: The Dynamic Thickened Flame (DTF) model

The Dynamic Thickened Flame (DTF) model [26] was employed to resolve the flame front on the LES grid. The unresolved flame wrinkling was modeled by the efficiency function of Charlette et al. [36].

The DTF model was validated on the three cases of Fig. 1 to verify that thickening has a reduced influence on both the propagation and autoignition mechanism. The test cases were simulated with AVBP on a DNS mesh ($\Delta x = 0.04$ mm) and on a coarser LES mesh ($\Delta x = 0.37$ mm). For the LES simulations thickening was applied, so that a minimum of 4.5 cells were located inside the flame front. For more details the reader is referred to [26].

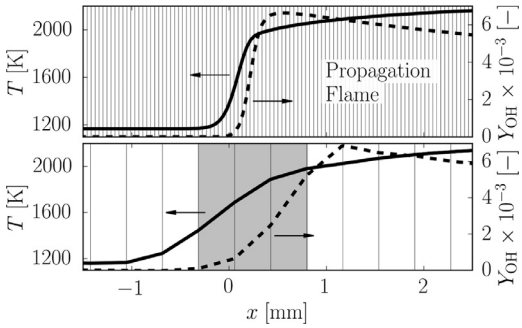

Fig. 4. Profiles of temperature and OH mass fraction in the 1-D stoichiometric propagating premixed flame (same case as Fig. 1a). Vertical lines: grid points. Top: DNS mesh. Bottom: LES with DTF. Gray area: thickened region with $F = 4.5$.

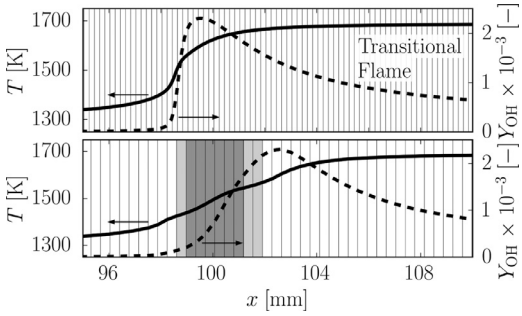

Fig. 5. Profiles of temperature and OH mass fraction in the 1-D transitional flame (same case as in Fig. 1c). Vertical lines: grid points. Top: DNS mesh with every 2nd grid point shown. Bottom: LES with DTF. Gray area: thickened region with F varying from 3.0 (light) to 4.5 (dark).

Figure 4 shows the profiles of temperature and OH mass fraction of case (a) of Fig. 1. Grid points are visualized with vertical lines. Based on the thermal flame thickness $\delta_{st} = 0.367$ mm, approximately nine cells were located inside the flame front with the DNS mesh (top graph), which corresponds to only one cell in the LES mesh (bottom graph). In order to resolve the flame on the LES mesh, the flame thickness was multiplied by a thickening factor of $F = 4.5$, while maintaining the correct laminar flame speed $s_L = 3.2$ m/s as for the DNS mesh. The thickening factor F was applied only in the flame region visualized in gray. Of course, when going from DNS to LES both profiles do not match exactly because the flame front is thickened on the LES grid. However as expected, the temperature and OH mass fraction gradients are significantly reduced in the flame region on the LES mesh, while their levels are correctly retrieved in the fresh and burnt gas.

Figure 5 shows the results for the transitional case (c) of Fig. 1. With an autoignition time of 14.1×10^{-3} s, derived from a PSR simulation, and an inlet velocity of 7.0 m/s, the autoignition point is

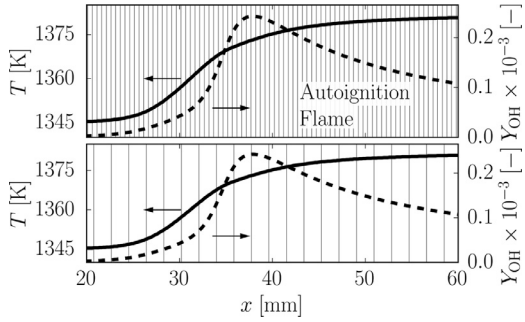

Fig. 6. Profiles of temperature and OH mass fraction in the 1-D autoignition case (same case as in Fig. 1d). Vertical lines: every 5th grid point shown. Top: DNS mesh. Bottom: LES with DTF.

located at the axial position $x_{AI} = 98.7$ mm. Defining the autoignition point in the simulations as $Y_{OH} = 10^{-3}$ (as done in [18] and [7]), this position is well retrieved on the DNS mesh (top graph). On the LES mesh (bottom graph) autoignition is slightly delayed due to the flame thickening, with a maximum error of 1% for this mesh size ($\Delta x = 0.37$ mm).

Finally, Fig. 6 presents the most reactive autoignition case (d) of Fig. 1. It is shown that with an autoignition time of 4.5×10^{-3} s (from PSR simulation in Fig. 3) and a inlet velocity of 7.0 m/s the autoignition point at $x_{AI,mr} = 31.5$ mm is well reproduced. In this case, species and temperature gradients are sufficiently small to be resolved on the LES mesh and no thickening is necessary.

4. Autoignition index (*AI*) applied to the Cabra flame

In the previous two sections only 0-D and 1-D cases were considered. One should note that the 3-D Cabra flame has an increased level of complexity with strong turbulence chemistry interactions in which, for example, time scales from a PSR simulations become meaningless. However in the following it is shown that numerical models and *AI* which have been validated with such simple cases are successfully applied to the flame.

4.1. Comparison to experiment

For the comparison to measurements, statistics were collected over 4 flow-through times.

Figure 7 presents the mean mixture fraction and temperature, the root mean square (rms) temperature and the mean mass fractions along the centerline, obtained for the fine and the coarse mesh presented in Subsection 3.2. Mixture fraction, mean and rms temperature, and CO_2 mass fraction are in very good agreement with experimental results for both meshes.

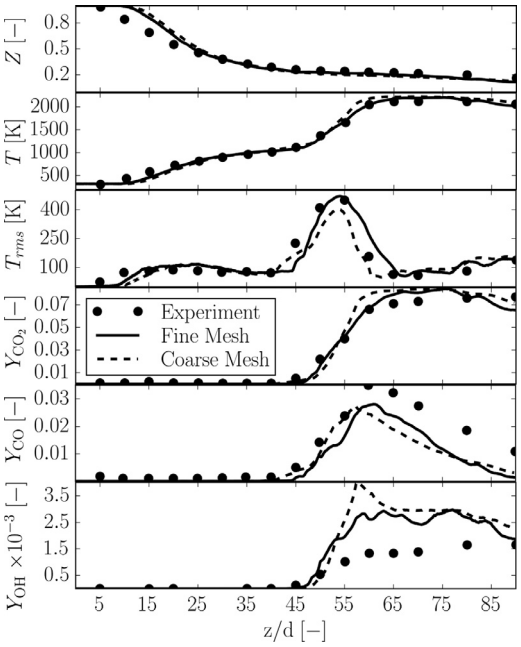

Fig. 7. Axial profiles of mean mixture fraction and temperature, rms temperature and mean mass fractions for CO_2, CO and OH (from top to bottom) along the centerline. Solid Lines: LES on the fine mesh. Dotted Lines: LES on the coarse mesh. Symbols: Experiment.

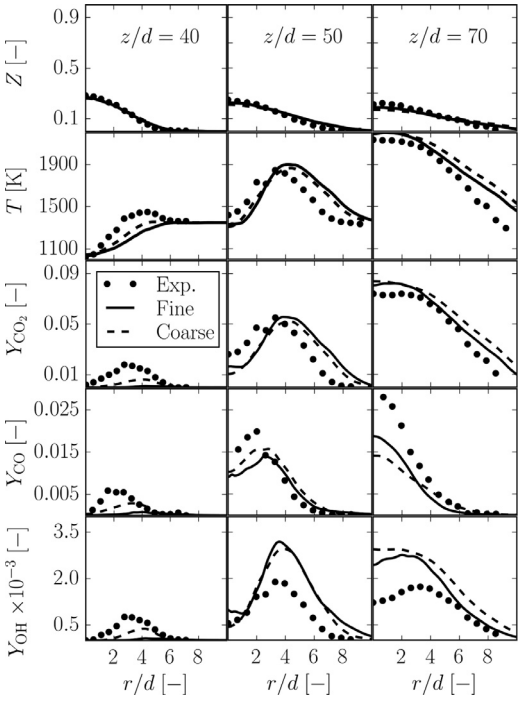

Fig. 8. Radial profiles of mean mixture fraction, temperature and mass fractions for CO_2, CO and OH (from top to bottom) at three axial positions. $z/d = 40$: onset of autoignition in the outer shear layer. $z/d = 50$: high heat release reaction zone. $z/d = 70$: post flame region (to be compared with Fig. 9). Solid Lines: LES on the fine mesh. Dotted Lines: LES on the coarse mesh. Symbols: Experiment.

Some underprediction of CO and overprediction of OH can be observed. However the same trend was already obtained by Cabra et al. [13] with reduced chemistry, Gkagkas and Lindstedt [22] and Navarro-Martinez and Kronenburg [23] with a detailed scheme as well as Ihme and See [18] with tabulated chemistry and can therefore not be attributed to the numerical methodology used in this work.

Mean radial profiles are obtained by averaging in time and in the circumferential direction. They are presented and compared to measurements at three axial positions in Fig. 8. The discrepancies appearing at $z/d = 40$ are linked to the 10% autoignition delay error, already mentioned in Subsection 3.2.1, and leading to the absence of temperature and species mass fractions peaks at this height. Further downstream, the profiles in the high heat release flame region at $z/d = 50$, and in the post flame region at $z/d = 70$ are in good agreement with experiment for both meshes.

4.2. Identification of burning regimes and stabilization mechanisms

The results shown in this subsection are derived on the fine mesh. Figure 9a and b shows instantaneous fields of heat release rate and temperature respectively, with a zoom on the spatial distribution of the flame thickening factor F in the inset in Fig. 9a. Weak heat release appears first at the jet border, starting at the nozzle exit down to $z/d \approx 45$ where a strong flame stabilizes and temperature suddenly increases. Further downstream, an intermediate post-flame zone develops.

The instantaneous and averaged distribution of AI are presented in Fig. 9e and d, conditioned on heat release rate and CH_2O concentration thresholds. This allows to focus on a reaction region which includes the upstream autoignition zone with relatively low heat release without displaying the post-flame chemistry region which is not of interest for the AI mapping.

CH_2O is formed during the autoignition process and drops with high temperature chemistry [22]. The isolines of low heat release rate (HR_{low}) and CH_2O thresholds used to condition the AI field, as well as the isoline of high heat release rate (HR_{high}), can be seen superimposed on the mean temperature field in Fig. 9c.

The instantaneous distribution of AI (e) allows to distinguish between autoignition, located close to the most reactive mixture fraction extending to the fuel side and propagation burning regime, oc-

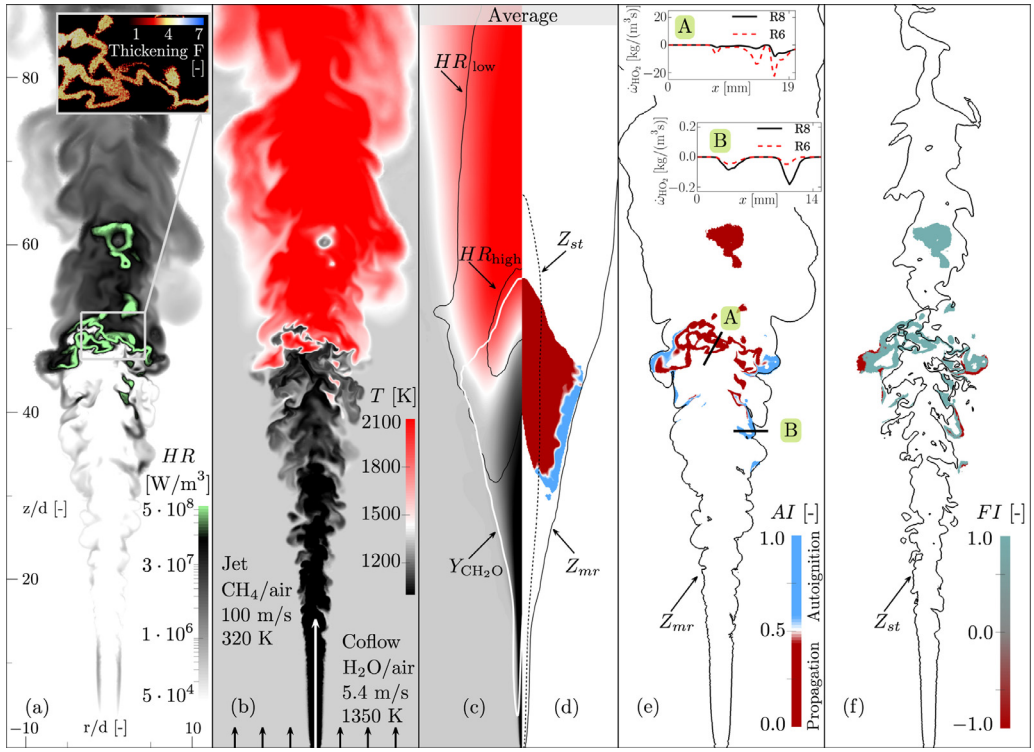

Fig. 9. Representative snapshots (same instant in time) in a cut of the 3-D domain of (a) heat release rate, (b) temperature, (e) autoignition index (*AI*) and (f) flame index (*FI*). Also in (a) inset with thickening factor F field. Low and high heat release rate isolines (resp. 10^6 and 10^8 W/m^3) and CH_2O mass fraction isoline (1×10^{-5}) are superimposed on (c) mean temperature field. The stoichiometric ($Z_{st} = 0.177$) and most reactive ($Z_{mr} = 0.00427$) mixture fraction isolines are superimposed on (d) the conditioned mean *AI* field. e): Most reactive mixture fraction isoline superimposed on instantaneous *AI* field. Insets A and B show the local contribution of R8 and R6 to HO_2 consumption. (f): Stoichiometric mixture fraction isoline superimposed on instantaneous *FI* field.

curring at high mixture fractions. For an autoignition kernel the change to a burnt state is rapid and propagation does not evolve. However as shown by Mastorakos et al. [37] the released heat at Z_{mr} diffuses towards richer mixture fractions, which become the most reactive ones and consequently auto-ignite until propagation flames emerge. The cuts A and B confirm that the contribution of R8 to HO_2 reaction rates is dominant over R6 in regions identified as autoignition by *AI* (B) and vice versa in regions identified as flame propagation (A).

The flame index (*FI*) is shown with the same thresholds in Fig. 9f. In its classical definition, with aligned gradients of fuel and oxidizer *FI* becomes 1 for premixed flames and with opposed gradients *FI* is −1 which is typical for diffusion flames. Figure 9f shows that *FI* is −1 in the very lean regions of the autoignition kernels. These regions are not aligned with the stoichiometric mixture fraction, and are located in low temperature, auto-igniting zones. Hence these are not diffusion flames, but correspond to the opposed mixing mode, as introduced by Yoo et al. [7]. Closer to the centerline, very lean premixed autoignition together with lean as well as rich premixed propagating flames can be observed, which is in agreement with the findings of Domingo et al. [12].

The averaged *AI* field in Fig. 9d confirms that autoignition is the dominating burning regime at the flame base. Note that instantaneous results at different instants in time (not shown here) as well as [23] show axial flame oscillations resulting in a wide axial spread of the averaged *AI*. In regions identified as propagation mode, axial velocities u range from 10 m/s in the outer jet up to 45 m/s close to the centerline. With $s_T/s_L \approx 1 + u'/s_L$ [38] (with rms velocity u') turbulent flame speeds s_T have estimated values of 7 m/s in the outer and 11 m/s in the inner jet and the premixed flame should be blown off. Autoignition however is able to anchor the flame, and appears therefore as the primary stabilization mechanism of this flame configuration. This is in line with the conclusions in [17,23,24] and with Cabra et al. [13] who numerically and experimentally showed a strong dependence of changing coflow temperatures on the lift-off height.

5. Conclusions

In the present paper a new criterion to distinguish between propagation flames and autoignition is introduced. Based on a reaction rate flux analysis for HO_2 chemistry, 2 reactions with distinct relative contributions for the two types of flames were identified. The autoignition index (*AI*) evaluating these relative contributions, provides useful insight into the reaction zone burning regimes.

The criterion was demonstrated with a CH_4/air turbulent lifted flame, simulated with LES, employing the DTF model and reduced chemistry. The numerical methodology was fully validated by comparisons with experiment and detailed chemistry calculations. Premixed and opposed mixing mode autoignition are identified as the dominant mechanism in the outer shear layer and at the flame base. Autoignition also appears as the driving mechanism for the flame stabilization in the high velocity flow. Note that the *AI* formulation can be applied to tabulated chemistry in combination with any turbulent combustion model, being either a PDF, CMC or DTF approach.

Acknowledgment

This research has been partially supported by the Swiss National Science Foundation under Grant 160579.

References

[1] F. Guethe, J. Hellat, P. Flohr, *J. Eng. Gas Turbines Power* 131 (2009).
[2] C. Prathap, F.C.C. Galeazzo, P. Kasabov, et al., *J. Eng. Gas Turbines Power* 134 (2012).
[3] T. Roediger, O. Lammel, M. Aigner, C. Beck, W. Krebs, *J. Eng. Gas Turbines Power* 135 (2013).
[4] A. Cavaliere, M. de Joannon, *Prog. Energy Combust. Sci.* 30 (2004) 329–366.
[5] A. Evulet, A.M. Elkady, A. Brand, D. Chinn, *Energy Procedia* 1 (2009) 3809–3816.
[6] H. Yamashita, M. Shimada, T. Takeno, *Proc. Combust. Inst.* 26 (1) (1996) 27–34.
[7] C.S. Yoo, R. Sankaran, J.H. Chen, *J. Fluid Mech.* 640 (2009) 453.
[8] R. Sullivan, B. Wilde, D.R. Noble, J.M. Seitzman, T.C. Lieuwen, *Combust. Flame* 161 (7) (2014) 1792–1803.
[9] J. Sidey, E. Mastorakos, *Proc. Combust. Inst.* 35 (3) (2015) 3537–3545.
[10] D. Ahrens, M. Kolb, C. Hirsch, T. Sattelmayer, *Proceedings of the ASME Turbo Expo (GT2015-42224)*, 2015.
[11] O. Colin, J.B. Michel, *Proc. Combust. Inst.* 35 (2) (2014) 1393–1399.
[12] P. Domingo, L. Vervisch, D. Veynante, *Combust. Flame* 152 (3) (2008) 415–432.
[13] R. Cabra, J.Y. Chen, R.W. Dibble, a.N. Karpetis, R.S. Barlow, *Combust. Flame* 143 (4) (2005) 491–506.
[14] N. Peters, *Prog. Energy Combust. Sci.* 10 (3) (1984) 319–339.
[15] J.B. Michel, O. Colin, C. Angelberger, D. Veynante, *Combust. Flame* 156 (7) (2009) 1318–1331.
[16] R. Mouangue, M. Obounou, L. Gomet, A. Mura, *Flow Turbul. Combust.* 92 (3) (2014) 731–765.
[17] M. Jangi, X. Zhao, D.C. Haworth, X.-S. Bai, *Combust. Flame* 162 (2) (2015) 408–419.
[18] M. Ihme, Y.C. See, *Combust. Flame* 157 (10) (2010) 1850–1862.
[19] N. Enjalbert, P. Domingo, L. Vervisch, *Combust. Flame* 159 (1) (2012) 336–352.
[20] R. Kulkarni, B. Bunkute, F. Biagioli, M. Duesing, W. Polifke, Proceedings of the ASME Turbo Expo (GT2014-26053), 2014, pp. 1–9.
[21] B. Fiorina, D. Veynante, S. Candel, *Flow Turbul. Combust.* (2014) 3–42.
[22] K. Gkagkas, R.P. Lindstedt, *Proc. Combust. Inst.* 31 (I) (2007) 1559–1566.
[23] S. Navarro-Martinez, A. Kronenburg, *Proc. Combust. Inst.* 32 (I) (2009) 1509–1516.
[24] R.L. Gordon, a.R. Masri, S.B. Pope, G.M. Goldin, *Combust. Theory Model.* 11 (3) (2007) 351–376.
[25] S. Navarro-Martinez, S. Rigopoulos, *Flow Turbul. Combust.* 87 (2–3) (2011) 407–423.
[26] O. Colin, F. Ducros, D. Veynante, T. Poinsot, *Phys. Fluids* 12 (7) (2000) 1843–1863.
[27] R.W. Bilger, S.H. Starner, R.J. Kee, *Combust. Flame* 80 (2) (1990) 135–149.
[28] E.L. Petersen, D.M. Kalitan, S. Simmons, G. Bourque, H.J. Curran, J.M. Simmie, *Proc. Combust. Inst.* 31 (I) (2007) 447–454.
[29] L.Y.M. Gicquel, N. Gourdain, J.F. Boussuge, et al., *C.R. Acad. Sci.* 339 (2–3) (2011) 104–124.
[30] O. Colin, M. Rudgyard, *J. Comput. Phys.* 162 (2) (2000) 338–371.
[31] F. Nicoud, F. Ducros, *Flow Turbul. Combust.* 62 (3) (1999) 183–200.
[32] T.J. Poinsot, S. Lele, *J. Comput. Phys.* 101 (1) (1992) 104–129.
[33] P. Pepiot-Desjardins, H. Pitsch, *Combust. Flame* 154 (1–2) (2008) 67–81.
[34] C.T. Bowman, R.K. Hanson, D.F. Davidson, et al., *GRI-Mech 2.11* (1997) available from http://www.me.berkeley.edu/gri-mech/.
[35] D.G. Goodwin, H.K. Moffat, R.L. Speth, 2015. URL: http://www.cantera.org.
[36] F. Charlette, C. Meneveau, D. Veynante, *Combust. Flame* 131 (1–2) (2002) 181–197.
[37] E. Mastorakos, T.A. Baritaud, T.J. Poinsot, *Combust. Flame* 109 (1–2) (1997) 198–223.
[38] Ö.L. Gülder, *Proc. Combust. Inst.* 23 (1) (1991) 743–750.